Chinese Journal of Natural Medicines

Discovery of bioactive polycyclic polyprenylated acylphloroglucinol from *Hypericum patulum* that protects against hepatic ischemia/reperfusion injury

Bo Tao, Xiangli Zhao, Zhengyi Shi, Jie Li, Yulin Duan, Xiaosheng Tan, Gang Chen, Changxing Qi, Yonghui Zhang

Citation: Bo Tao, Xiangli Zhao, Zhengyi Shi, Jie Li, Yulin Duan, Xiaosheng Tan, Gang Chen, Changxing Qi, Yonghui Zhang, Discovery of bioactive polycyclic polyprenylated acylphloroglucinol from *Hypericum patulum* that protects against hepatic ischemia/reperfusion injury, Chinese Journal of Natural Medicines, 2025, 23(9), 1104−1110. doi: 10.1016/S1875−5364(25)60975−7.

View online: https://doi.org/10.1016/S1875−5364(25)60975−7

Chinese Journal of Natural Medicines 23 (2025) 1104-1110

Contents lists available at ScienceDirect

Chinese Journal of Natural Medicines

journal homepage: www.cjnmcpu.com/

Original article

Discovery of bioactive polycyclic polyprenylated acylphloroglucinol from *Hypericum patulum* that protects against hepatic ischemia/reperfusion injury

Bo Tao[a,c,Δ], Xiangli Zhao[b,Δ], Zhengyi Shi[a,Δ], Jie Li[a], Yulin Duan[d], Xiaosheng Tan[b,*], Gang Chen[b,*], Changxing Qi[a,b,*], Yonghui Zhang[a,*]

[a] *Hubei Key Laboratory of Natural Medicinal Chemistry and Resource Evaluation, Tongji Medical College, Huazhong University of Science and Technology, Wuhan 430030, China*
[b] *Key Laboratory of Organ Transplantation, Ministry of Education; NHC Key Laboratory of Organ Transplantation; Key Laboratory of Organ Transplantation, Chinese Academy of Medical Sciences, Wuhan 430030, China*
[c] *Department of Pharmacy, Union Hospital, Tongji Medical College, Huazhong University of Science and Technology, Wuhan 430022, China*
[d] *Department of Pharmacy, Wuhan No. 1 Hospital, Wuhan 430022, China*

ARTICLE INFO

Article history:
Received 24 October 2024
Revised 7 January 2025
Accepted 23 February 2025
Available online 20 September 2025

Keywords:
Hepatic ischemia/reperfusion injury
Hypericum patulum
Polycyclic polyprenylated acylphloroglucinols
Natural products
Secondary metabolites

ABSTRACT

Hepatic ischemia/reperfusion injury (IRI) remains a critical complication contributing to graft dysfunction following liver surgery. As part of an ongoing search for hepatoprotective natural products, five previously unreported homoadamantane-type polycyclic polyprenylated acylphloroglucinols (PPAPs), named hyperhomanoons A–E (**1**–**5**), and one known analog, hypersampsone O (**6**), were isolated from *Hypericum patulum*. Among these, compound **6** demonstrated potent protective effects against $CoCl_2$-induced hypoxic injury in hepatocytes. Furthermore, in a murine model of hepatic IRI induced by vascular occlusion, pretreatment with **6** markedly alleviated liver damage and reduced hepatocyte apoptosis. This study is the first to identify PPAPs as promising scaffolds for the development of therapeutic agents targeting hepatic IRI, underscoring their potential as lead compounds in drug discovery efforts for ischemic liver diseases.

1. Introduction

Hepatic ischemia/reperfusion injury (IRI) is a major clinical challenge encountered during liver transplantation and hepatic surgeries. It occurs when the blood supply to the liver is temporarily interrupted and then restored, triggering a cascade of pathophysiological events that can lead to severe liver dysfunction, intrahepatic cholestasis, systemic inflammatory response syndrome, and multiple organ failure [1-4]. Despite intensive research, the mechanisms underlying IRI remain incompletely elucidated. Current evidence implicates a complex interplay of anaerobic metabolism, immune activation, mitochondrial injury, regulated cell death pathways, oxidative stress, and the dysregulated production of cytokines and chemokines [5-10]. This mechanistic complexity has hampered the development of effective therapeutic strategies. Currently used interventions, such as glutathione supplementation aimed at reducing oxidative stress, often yield limited clinical benefit due to issues like rapid metabolism and low bioavailability [11-13]. Consequently, there is a pressing need for novel compounds with robust and multi-targeted hepatoprotective effects.

Natural products continue to be a rich source of pharmacologically active lead compounds for liver diseases. Several natural agents, such as baicalin, 5α-stigmast-3,6-dione, notoamide Q, anethole, and plumbagin, have demonstrated protective effects in murine models of hepatic IRI [14]. Among these, polycyclic polyprenylated acylphloroglucinols (PPAPs) have emerged as structurally unique secondary metabolites with diverse bioactivities, including anti-inflammatory, antioxidant, immunosuppressive, and neuroprotective properties [15-23]. In pursuit of hepatoprotective natural products [24-27], five homadamantane-type PPAPs, hyperhomanoons A–E (**1**–**5**), and one known PPAP hypersampsone O (**6**) [28] were isolated from *Hypericum patulum* (Fig. 1). Preliminary biological evaluation revealed that hypersampsone O (**6**) exhibited potent cytoprotective activity against $CoCl_2$-induced hypoxic injury in hepatocytes. Furthermore, in a murine model of hepatic IRI, pretreatment with compound **6** significantly mitigated liver tissue injury and reduced hepatocyte apoptosis. In this study, we report detailed information on the extraction, isolation, structure elucidation, and hepatoprotective bioactivity profiles of **1**–**6**.

2. Result and discussion

Hyperhomanoon A (**1**) was obtained as a colorless crystal. Its molecular formula was determined as $C_{31}H_{44}O_5$ based on high-resolution electrospray ionization mass spectrometry (HR-ESI-

* Corresponding author.
E-mail addresses: txs900416@163.com (X. Tan); gchen@tjh.tjmu.edu.cn (G. Chen); qichangxing@hust.edu.cn (C. Qi); zhangyh@mails.tjmu.edu.cn (Y. Zhang)
Δ These authors contributed equally to this work.

https://doi.org/10.1016/S1875-5364(25)60975-7

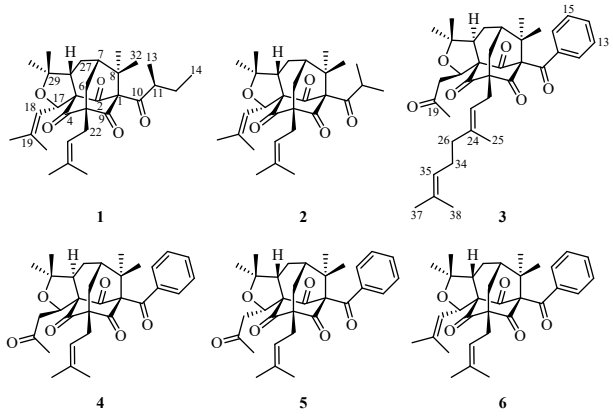

Fig. 1 Chemical structures of compounds **1**–**6**.

MS) at *m/z* 519.3074 [M + Na]$^+$ (Calcd. for 519.3086), indicating ten degrees of unsaturation. The ^{1}H NMR spectrum of **1** showed characteristic signals of two olefinic protons (δ_H 5.35, d, *J* = 9.0; 5.21, t, *J* = 7.4) and 10 methyl singlets (δ_H 1.73, s; 1.72, s; 1.64, s; 1.62, s; 1.37, s; 1.27, s; 1.26, s; 1.24, s; 1.10, d, *J* = 6.4; 0.76, t, *J* = 7.4) (Table 1). The ^{13}C nuclear magnetic resonance (NMR) and distortionless enhancement by polarization transfer (DEPT) spectra of **1** showed the presence of ten methyls (δ_C 31.1, 26.3, 26.2, 25.2, 24.6, 22.1, 18.8, 18.2, 17.2, 11.8), four methylenes (δ_C 34.9, 28.7, 26.4, 25.6), six methines (δ_C 120.1, 118.7, 74.7, 55.0, 51.5, 42.5), and eleven quaternary carbons (δ_C 207.7, 204.1, 202.5, 199.7, 139.5, 135.8, 86.6, 83.1, 77.0, 67.9, 46.7) (Table 2). The above data suggested that **1** is a PPAP featuring a homoadamantane skeleton.

The planar structure of **1** was determined through extensive 2D NMR analysis. Key heteronuclear multiple bond correlations (HMBCs) from H-17 to C-3 and C-4; from H_2-22 to C-4, C-5, C-6, and C-9; from H-28 to C-2 and C-3; from H_3-32/H_3-33 to C-1, C-7, and C-8, coupled with the ^{1}H–^{1}H correlation spectroscopy (COSY) correlations of H_2-6/H-7/H_2-27/H-28 suggested **1** possess a rigid homoadamantane framework (Fig. 2). The downfield chemical shifts of C-17 (δ_C 74.4) and C-29 (δ_C 83.1) combined with the molecular unsaturation count, suggested the incorporation of a fused furan ring (C-3–C-17–O–C-29–C-28) (Fig. 2). This structural motif was unequivocally confirmed by single-crystal X-ray diffraction analysis (Fig. 3).

Based on the conformation of the highly rigid homoadamantane architecture, the relative configurations at C-1, C-3, C-5, and C-7 of **1** were set up as the former literature reported [43], and the relative configurations of C-17 and C-28 were identified by its NOESY spectrum. In the NOESY data, the correlations of H-17/H-28/H-6b indicated that H-17 and H-28 were on the same side and assigned to be *β*-orientated (Fig. S1). Finally, the single-crystal X-ray diffraction experiment definitely confirmed the relative configuration of **1** and also confirmed its absolute configuration [Flack parameter −0.05 (4); CCDC number 2279825] (Fig. 3).

Hyperhomanoon B (**2**) was obtained as a colorless oil. Its molecular formula, $C_{30}H_{42}O_5$, was determined *via* HR-ESI-MS (*m/z* 505.2926 [M + Na]$^+$, Calcd. for 505.2930), suggesting ten degrees of unsaturation. Comparison of its NMR spectra with those of **1** indicated a highly similar structural framework, except for the substitution of a *sec*-butyl group (δ_C 51.5, 26.4, 11.8, 17.2) at C-10 in **1** with an isopropyl group (δ_C 44.3, 21.1, 20.7) in **2**. This modification was confirmed by ^{1}H–^{1}H COSY correlations of H_1-11/H_3-12/H_3-13 (Fig. 2). Consistent NOESY correlations and the preserved homoadamantane core further supported that **2** shared the same relative configuration as **1** (Fig. S1). The absolute configuration of **2** was determined by comparing its experimental electronic circular dichroism (ECD) spectrum with that of **1**, showing excellent agreement (Fig. 4).

Hyperhomanoon C (**3**) was assigned the molecular formula $C_{37}H_{46}O_6$ based on HR-ESI-MS, which showed a molecular ion peak consistent with the calculated value. Comparative NMR analysis revealed a close structural similarity to the known compound hyphenrone [29]. However, detailed HMBC and ^{1}H–^{1}H COSY spectra suggested the presence of a propan-2-one group (δ_C 44.0, 206.6, 30.7) at C-17 in **3**, replacing the 2-methylprop-1-ene group in hyphenrone O (δ_C 121.3, 139.1, 26.8, 18.5). This assignment was corroborated by HMBCs from H_3-20 to C-18 and C-19 and the ^{1}H–^{1}H COSY correlation of H-17/H_2-18 (Fig. 2). The relative configuration was established *via* nuclear Overhauser effect spectroscopy (NOESY) correlations of H_2-6/H_3-32, H-17/H-28, and H-28/H_3-33 (Fig. S1). The absolute configuration was subsequently confirmed by single-crystal X-ray diffraction [Flack parameter 0.11 (5); CCDC number 2280661] (Fig. 3).

Hyperhomanoon D (**4**), a colorless oil, was determined to have the molecular formula $C_{32}H_{38}O_6$ based on its HR-ESI-MS data (*m/z* 541.2552 [M + Na]$^+$, Calcd. for 541.2566). NMR analyses indicated a planar structure similar to that of compound **3**, with the key difference being the substitution of a geranyl group at C-5 in **3** with an isopentenyl unit δ_C 29.6, 119.5, 134.4, 26.2, 18.2) in **4**. This modification was confirmed by HMBCs from H_3-25/H_3-26 to C-24 and C-23, from H_2-22 to C-4, C-5 and C-9, as well as the H_2-22/H-23 COSY spin system (Fig. 2). The NOESY correlations observed at H-17/H-28/H_3-33 and H_3-32/H-6a suggested suggested *α*-orientations for both H-17 and H-28 (Fig. S1). The absolute configuration was determined as 1*R*,3*S*,5*S*,7*S*, 17*R*,28*S* and TDDFT-calculated ECD spectra (Fig. 4).

Hyperhomanoon E (**5**) shared an identical planar structure with **4**, as evidenced by its HR-ESI-MS and NMR spectral data. Key NOESY correlations of H-17/H-28/H-6a and H-6b/H_3-32 indicated that H-17 and H-28 were on the same *β*-face of the molecule (Fig. S1). The absolute configuration was validated by comparison of experimental and calculated ECD spectra, further confirming the stereostructure (Fig. 4).

To evaluate their hepatoprotective potential, compounds **1**–**6** were screened for anti-hypoxic activity using a $CoCl_2$-induced damage model in AML-12 mouse hepatocytes [30-34]. T cell viability was assessed by the CCK-8 assay. Among the six compounds, only hypersampsone O (**6**) exhibited notable cytoprotective activity, significantly improving cell survival in a dose-dependent manner at concentrations ranging from 0.39 to 25 μmol·L^{-1} (Figs. 5A and 5B). In addition, compound **6** displayed no observable cytotoxicity in normal AML-12 cells within the same concentration range (Fig. 5C).

The hepatic vessel-interrupted mice model is an effective animal model for studying HIRI, which can effectively simulate the pathogenesis of human HIRI and evaluate a new therapeutic drug for this disease [35-37]. To quantitatively evaluate liver injury, serum levels of alanine aminotransferase (ALT), aspartate aminotransferase (AST), and lactate dehydrogenase (LDH) were measured, as these enzymes are clinically recognized biomarkers of hepatocellular damage. As shown in Fig. 6A, pretreatment with compound **6** resulted in a significant reduction in ALT, AST, and LDH levels compared to the untreated HIRI group.

The hematoxylin and eosin (H&E) staining was a classical method for evaluating the liver tissue damage [38-40], while TUNEL staining and cleaved caspase-3 immunohistochemistry were employed to detect apoptotic cells, reflecting key biochemical and morphological features of programmed cell death [41-45]. As shown in Figs. 6B and 6C, the untreated IRI group exhibited extensive hepatic necrosis and a high degree of apoptosis. In contrast, mice pretreated with compound **6** demonstrated markedly reduced tissue damage and apoptotic activity, indicating a substantial protective effect. As shown in Figs. 6D and 6E, pretreatment with compound **6** significantly reduced the number of MPO-positive cells compared to the IRI group, suggesting that **6** also mitigated hepatic inflammation.

Table 1 ^{1}H NMR data for compounds **1**–**5** (*J* in Hz).

No.	**1** [a]	**2** [a]	**3** [a]	**4** [a]	**5** [b]
6a	2.44, dd (14.7, 6.9)	2.45, dd (15.0, 6.6)	2.56, m	2.53, m	2.11, m
6b	1.91, m	1.92, d (15.0)	1.76, m	1.75, m	2.54, m
7	1.95, m	1.97, m	2.12, m	2.13, m	2.09, m
11	1.47, m	1.78, m			
12a	1.89, m	1.10, d (6.4)	7.50, m	7.52, d (7.3)	7.14, m
12b	1.32, m				
13	0.76, t (7.4)	1.09, d (6.4)	7.27, t (8.1)	7.28, t (7.9)	7.29, t (8.2)
14	1.10, d (6.4)		7.38, t (7.5)	7.39, t (7.4)	7.41, t (7.4)
15			7.27, t (8.1)	7.28, t (7.9)	7.29, t (8.2)
16			7.50, t (7.5)	7.52, d (7.3)	7.14, m
17	5.58, d (9.0)	5.57, d (9.0)	5.05, dd (7.7, 6.4)	5.06, t (7.1)	5.11, dd (9.6, 3.0)
18a	5.35, d (9.0)	5.35, d (9.0)	3.16, dd (17.0, 7.7)	3.15, dd (17.0, 7.4)	2.55, m
18b			2.78, dd (17.0, 6.4)	2.81, dd (17.0, 6.6)	2.12, m
20	1.62, s	1.63, s	2.07, s	2.08, s	2.00, s
21	1.73, s	1.75, s			
22a	2.51, d (7.4)	2.51, d (7.5)	2.60, m	2.58, m	2.64, dd (15.1, 7.5)
22b	2.51, d (7.4)	2.51, d (7.5)		2.58, m	2.59, dd (15.1, 7.5)
23	5.21, t (7.4)	5.22, t (7.5)	5.08, m	5.03, m	5.26, t (6.1)
25	1.72, s	1.73, s	1.68, s	1.67, s	1.75, s
26	1.64, s	1.64, s	1.95, m	1.67, s	1.68, s
27a	2.11, dd (15.2, 12.4)	2.12, dd (15.1, 11.7)	2.33, dt (16.4, 8.4)	2.33, m	2.18, m
27b	1.77, m	1.76, m	1.58, m	1.59, m	1.84, dd (8.6, 6.5)
28	2.38, dd (11.1, 8.1)	2.38, dd (11.9, 8.4)	2.51, dd (11.1, 9.5)	2.50, m	2.42, dd (11.7, 8.6)
30	1.37, s	1.37, s	1.32, s	1.31, s	1.34, s
31	1.26, s	1.26, s	1.15, s	1.16, s	1.15, s
32	1.24, s	1.24, s	1.45, s	1.45, s	1.43, s
33	1.27, s	1.28, s	1.51, s	1.52, s	1.38, s
34			2.04, m		
35			5.07, m		
37			1.58, s		
38			1.66, s		

[a] Recorded at 400 MHz in $CDCl_3$; [b] Recorded at 600 MHz in $CDCl_3$.

3. Experimental

3.1. General experimental procedures

The dried leaves of *H. patulum* (20 kg) were extracted with 95% ethanol at room temperature. The ethanol extract was concentrated under reduced pressure to afford a crude residue, which was suspended in water and subsequently partitioned with dichloromethane. The dichloromethane-soluble portion (1.5 kg) was subjected to silica gel column chromatography (CC) (100–200 mesh) using a petroleum ether/ethyl acetate gradient (70∶1 to 1∶1, *V/V*), yielding seven main fractions (Fr. 1–Fr. 7). Fr. 5 (100 g) was rechromatographed on silica gel (200–300 mesh) with the same eluent system (100∶1 to 1∶1, *V/V*), affording five subfractions (Fr. 5.1–Fr. 5.5). Fr. 5.2 was separated *via* Sephadex LH-20 CC (CH_2Cl_2–MeOH), resulting in six further subfractions (Fr. 5.2.1–Fr. 5.2.6). Fr. 5.2.4 was further purified by repeated semipreparative HPLC (CH_3OH–H_2O, *V/V*, 85∶15, 3 mL·min^{-1}) to yield **1** (t_R 32 min, 15.03 mg), **2** (t_R 28 min, 26.45 mg) and **6** (t_R 23 min, 10.75 mg). Similarly, Fr. 6 (150.0 g) was subjected to silica gel CC (200–300 mesh) and eluted with petroleum ether ethyl acetate (100∶1–1∶1), and divided into eight fractions (Fr. 6.1–Fr. 6.8). Fr. 6.5 was further separated using Sephadex LH-20 281 (CH_2Cl_2–MeOH) to obtain three fractions (Fr. 6.5.1–Fr. 6.5.3). Fr. 6.5.3 was further separated on an ODS column (MeOH–H_2O, *V/V*, 20∶80–100∶0) to yield ten fractions (Fr. 6.5.3.1–Fr. 6.5.3.10). Fr. 6.5.3.2 was further purified by repeated semipreparative HPLC (MeOH–H_2O, *V/V*, 80∶20, 3 mL·min^{-1}) separations to yield **3** (t_R 42 min, 4.55 mg), **4** (t_R 35 min, 7.84 mg) and **5** (t_R 37 min, 4.25 mg).

3.2. Spectroscopic data

Hyperhomanoon A (**1**): colorless crystal; mp: 170–172 °C; $[\alpha]_D^{25}$ +6.2 (*c* 0.3, MeOH); UV (MeOH) λ_{max} (log ε) 203 (4.14) nm; ECD (MeOH) λ_{max} ($\Delta\varepsilon$) 204 (−4.01), 208 (−1.82), 216 (−1.36), 221 (−2.92) 234 (−0.062), 259 (−2.99), 288 (+0.46), 294 (+0.26), 302

Table 2 ^{13}C NMR data for compounds **1**–**5** (*J* in Hz).

No.	**1** [a]	**2** [a]	**3** [a]	**4** [a]	**5** [b]
1	86.6, C	86.5, C	82.9, C	82.8, C	83.2, C
2	199.7, C	199.6, C	202.5, C	202.5, C	200.0, C
3	77.0, C	77.0, C	74.3, C	74.3, C	75.1, C
4	202.5, C	202.4, C	202.5, C	202.6, C	202.6, C
5	67.9, C	67.9, C	68.4, C	68.4, C	68.4, C
6	34.9, CH_2	34.9, CH_2	46.2, CH_2	46.4 CH_2	35.7, CH_2
7	42.5, CH	42.4, CH	44.2, CH	44.1 CH	42.5, CH
8	46.7, C	46.7, C	52.1, C	52.2, C	48.3, C
9	204.1, C	204.1, C	204.3, C	204.4, C	203.8, C
10	207.7, C	207.9, C	194.4, C	194.5, C	194.1, C
11	51.5, CH	44.3, CH	136.9, C	136.8, C	137.1, C
12	26.4, CH_2	21.1, CH_3	129.6, CH	129.7, CH	128.3, CH
13	11.8, CH_3	20.7, CH_3	127.7, CH	127.7, CH	128.6, CH
14	17.2, CH_3		131.9, CH	131.9, CH	132.1, CH
15			127.7, CH	127.7, CH	128.6, CH
16			129.6, CH	129.7, CH	128.3, CH
17	74.7, CH	74.7, CH	74.9, CH	74.9, CH	73.5, CH
18	120.2, C	119.8, CH	44.0, CH_2	44.1, CH_2	43.5, CH_2
19	139.5, C	140.0, C	206.6, C	206.6, C	205.7, C
20	26.3, CH_3	26.3, CH_3	30.7, CH_3	30.6, CH_3	30.7, CH_3
21	18.8, CH_3	18.8, CH_3			
22	28.7, CH_2	28.7, CH_2	29.5, CH_2	29.6, CH_2	29.1, CH_2
23	118.8, CH	118.7, CH	119.2, CH	119.5, CH	118.6, CH
24	135.8, C	135.8, C	138.2, C	134.4, C	135.8, C
25	26.2, CH_3	26.2, CH_3	16.6, CH_3	26.2, CH_3	26.3, CH_3
26	18.2, CH_3	18.2, CH_3	40.2, CH_2	18.2, CH_3	18.3, CH_3
27	25.6, CH_2	25.6, CH_2	29.9, CH_2	29.9, CH_2	25.4, CH_2
28	55.0, CH	54.8, CH	54.7, CH	54.7, CH	53.5, CH
29	83.1, C	83.0, C	83.6, C	83.6, C	82.9, C
30	31.1, CH_3	31.1, CH_3	31.2, CH_3	31.2, CH_3	30.5, CH_3
31	25.2, CH_3	25.3, CH_3	24.0, CH_3	23.9, CH_3	25.2, CH_3
32	24.6, CH_3	24.6, CH_3	26.5, CH_3	26.5, CH_3	25.3, CH_3
33	22.1, CH_3	22.2, CH_3	23.0, CH_3	23.0, CH_3	22.7, CH_3
34			26.9, CH_2		
35			124.4, CH		
36			131.6, C		
37			17.9, CH_3		
38			25.9, CH_3		

[a] Recorded at 100 MHz in $CDCl_3$; [b] Recorded at 150 MHz in $CDCl_3$

(+0.91), 306 (+0.80) and 314 (+2.12) nm; IR (KBr) ν_{max} 2967, 2921, 2851, 1728, 1697, 1454, 1382, 1235, 1219 and 1066 cm^{-1}; the data of ^1H and ^{13}C NMR (Tables 1 and 2); HR-ESI-MS *m/z* 519.3074 ($[M + Na]^+$, Calcd. for $C_{31}H_{44}O_5Na^+$, 519.3086).

Hyperhomanoon B (**2**): colorless oil; $[\alpha]_D^{25}$ +45.0 (*c* 0.1, MeOH); UV (MeOH) λ_{max} (log ε) 202 (4.23) nm; ECD (MeOH) λ_{max} ($\Delta\varepsilon$) 202 (−4.47), 213 (−0.48), 221 (−1.45), 237 (+0.34), 259 (−1.45), 274 (−0.55), 293 (−1.83) and 316 (+3.07) nm; IR (KBr) ν_{max} 2968, 2922, 2852, 1728, 1691, 1660, 1632, 1469, 1451, 1380, 1236, 1217 and 1066 cm^{-1}; the data of ^1H and ^{13}C NMR

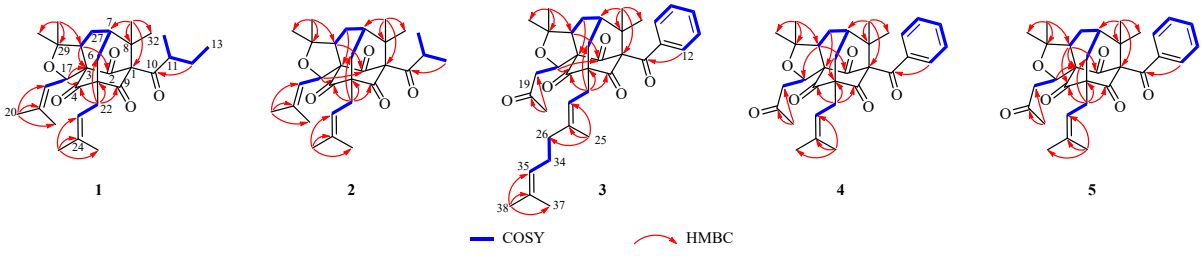

Fig. 2 Key 2D correlations of **1**–**5**.

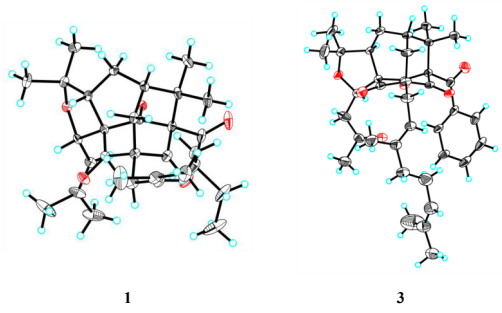

Fig. 3 X-ray crystal structure of **1** and **3**.

(Tables 1 and 2); HR-ESI-MS *m/z* 505.2926 ([M + Na]$^+$, Calcd. for $C_{30}H_{42}O_5Na^+$, 505.2930).

Hyperhomanoon C (**3**): colorless crystal; mp: 128–129 °C; $[\alpha]_D^{25}$ +26.2 (*c* 0.4, MeCN); UV (MeCN) λ_{max} (log ε) 246 (3.91) nm; ECD (MeCN) λ_{max} ($\Delta\varepsilon$) 205 (−3.06), 214 (+2.12), 240 (−0.45), 248 (+0.64), 261 (−0.84), 280 (+0.49) and 321 (−0.44) nm; IR (KBr) ν_{max} 2972, 2928, 1698, 1449, 1376, 1248, 1226 and 1072 cm^{-1}; the data of ^{1}H and ^{13}C NMR (Tables 1 and 2); HR-ESI-MS *m/z* 609.3170 ([M + Na]$^+$, Calcd. for $C_{37}H_{46}O_6Na^+$, 609.3190).

Hyperhomanoon D (**4**): colorless oil; $[\alpha]_D^{25}$ +95.3 (*c* 0.4, MeOH); UV (MeOH) λ_{max} (log ε) 245 (3.85) nm; ECD (MeOH) λ_{max} ($\Delta\varepsilon$) 206 (+3.56), 220 (+0.06), 229 (+0.55), 236 (−0.06), 240 (+0.39), 261 (−1.24), 287 (+0.46), 306 (−0.62) and 327 (−0.63) nm; IR (KBr) ν_{max} 2968, 2922, 2852, 1733, 1697, 1468, 1449, 1248, 1226 and 1074 cm^{-1}; the data of ^{1}H and ^{13}C NMR (Tables 1 and 2); HR-ESI-MS *m/z* 541.2552 ([M + Na]$^+$, Calcd. for $C_{32}H_{38}O_6Na^+$, 541.2566).

Hyperhomanoon E (**5**): colorless oil; $[\alpha]_D^{25}$ −2.90 (*c* 0.5, MeOH); UV (MeOH) λ_{max} (log ε) 246 (3.86) nm; ECD (MeOH) λ_{max} ($\Delta\varepsilon$) 210 (−1.62), 247 (+5.82) and 308 (−1.41) nm; IR (KBr) ν_{max} 2962, 2924, 2853, 1735, 1703, 1448, 1384 and 1236 cm^{-1}; the data of ^{1}H and ^{13}C NMR (Tables 1 and 2); HR-ESI-MS *m/z* 541.2569 ([M + Na]$^+$, Calcd. for $C_{32}H_{38}O_6Na^+$, 541.2566).

3.3. X-ray crystallographic analysis

Single crystals of **1** were obtained from methanol/water (10∶1) at 4 °C, with CCDC No. 2279825, and single crystals of **3** were obtained from methanol/water (10∶2) at 4 °C, with CCDC No. 2280661.

Crystal data for hyperhomanoon A (**1**): $C_{31}H_{44}O_5$, *Mr* = 496.66, *a* = 13.252 20 (10) Å, *b* = 13.570 60 (10) Å, *c* = 16.136 60 (10) Å, α = 90°, β = 90°, γ = 90°, *V* = 2902.01 (4) Å^3, *T* = 293 (2) K, space group *P* 212 121, *Z* = 4, μ(Cu Kα) = 0.598 mm^{-1}, θ_{max} = 74.243, 34103 reflections measured, 5840 independent reflections (R_{int} = 0.0326). The final R_1 values were 0.0448 [$I > 2\sigma(I)$]. The final $wR(F^2)$ values were 0.1249 [$I > 2\sigma(I)$]. The final R_1 values were 0.0454 (all data). The final $wR(F^2)$ values were 0.1255 (all data). The goodness of fit on F^2 was 1.082. Flack parameter = −0.05 (4).

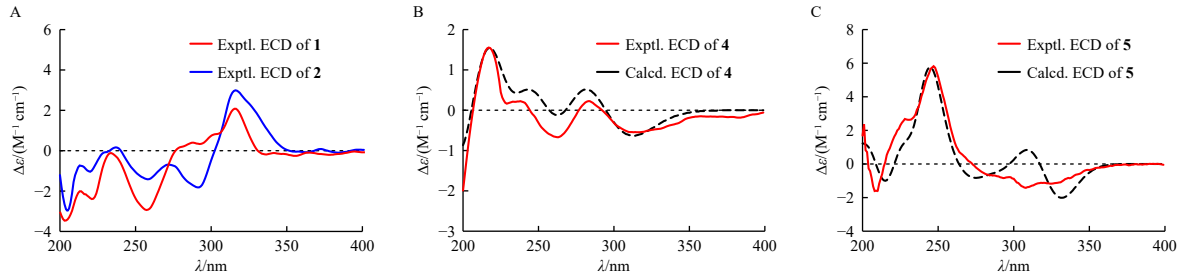

Fig. 4 (A) Experimental ECD spectra of **1** and **2**. (B) Experimental and calculated ECD data of **4**; (C) Experimental and calculated ECD data of **5**.

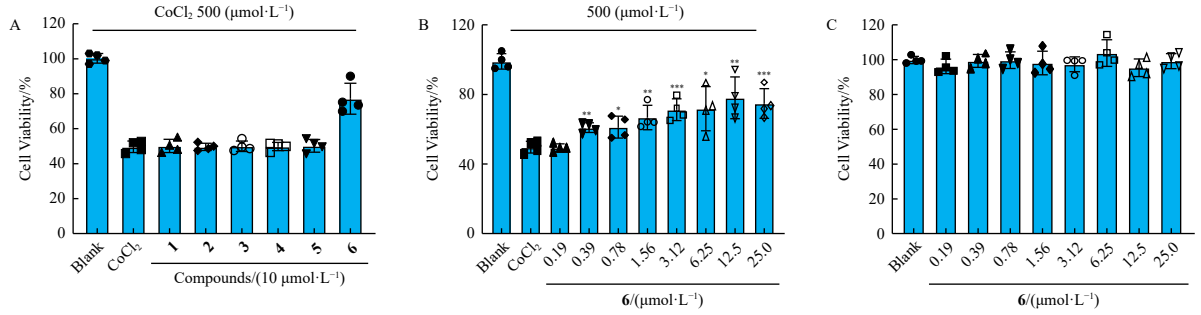

Fig. 5 (A) Protective effects of **1**–**6** against $CoCl_2$-induced hypoxic injury in AML-12 hepatocytes. (A) AML-12 cells were pretreated with compounds **1**–**6** (10 μmol·L^{-1}) for 1 h, followed by exposure to $CoCl_2$ (500 μmol·L^{-1}) for 24 h. Cell viability was assessed using the CCK-8 assay. (B) Dose-dependent protective effects of compound **6** were evaluated at concentration ranging from 0.19 to 25 μmol·L^{-1} in $CoCl_2$-treated AML-12 cells. (C) Cytotoxicity of compound **6** was assessed in untreated AML-12 cells at concentrations ranging from 0.19 to 25.0 μmol·L^{-1} to confirm safety in normal conditions. Data were expressed as the mean ± SEM (n = 4). *P < 0.05, **P < 0.01, ***P < 0.001 *vs* control group.

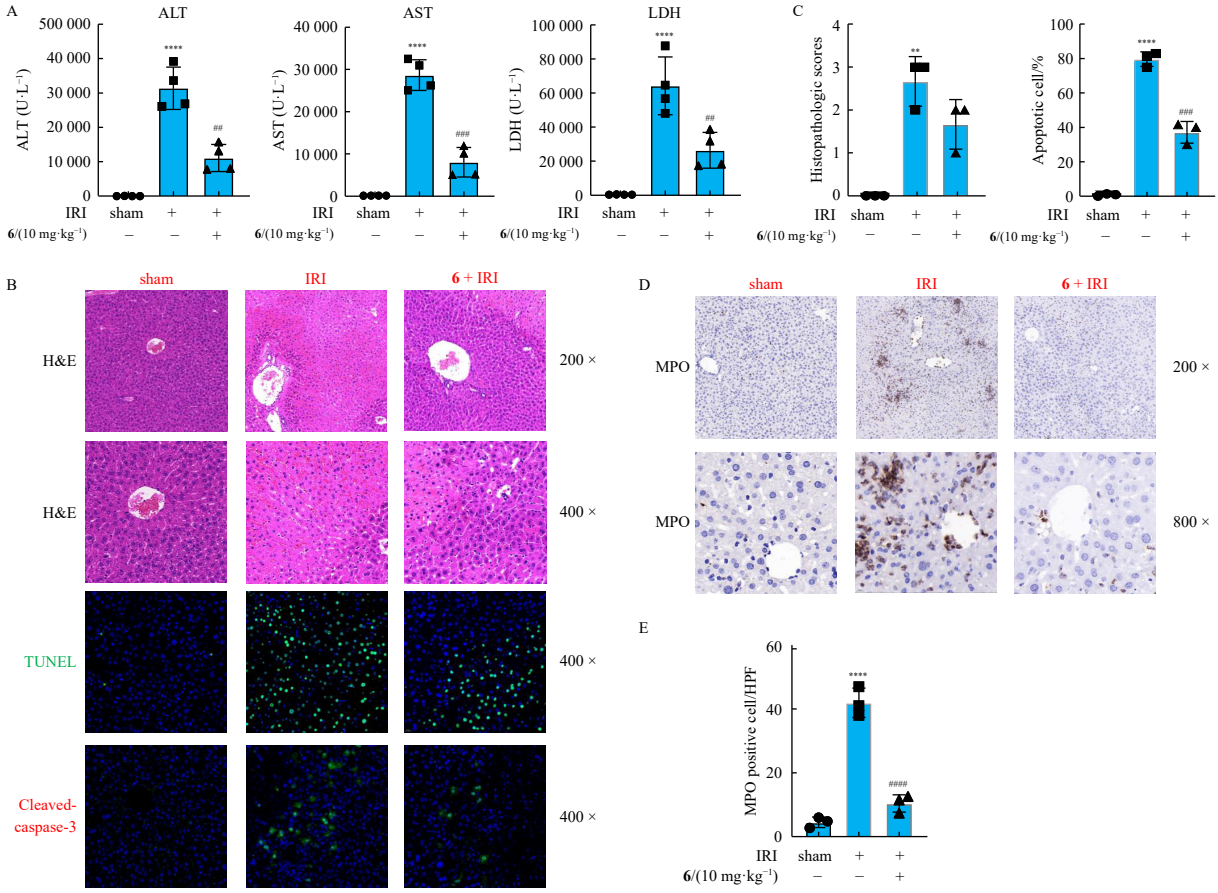

Fig. 6 Hepatoprotective and anti-apoptotic effects of compound **6** in a murine HIRI model. (A) Serum levels of ALT, AST, and LDH in the negative control group, HIRI group, and **6**-pretreated group (n = 4). (B) Representative histological images of liver sections stained with H&E, TUNEL, and cleaved caspase-3 staining to evaluate liver injury in mice. Asterisks indicate regions of hepatic ecchymosis; triangles denote leukocyte infiltration. (C) Quantitative analysis of liver injury based on Suzuki's histological score and TUNEL-positive apoptotic cell percentages (n = 3). (D) Immunohistochemical analysis of MPO expression revealed reduced inflammatory infiltration in liver tissues of mice pretreated with **6**. (E) Quantification of MPO-positive cells per field of view. All data represent mean ± SEM from at least three independent experiments. $^{**}P$ < 0.01, $^{****}P$ < 0.0001 *vs* the control group; $^{\#\#}P$ < 0.01, $^{\#\#\#}P$ < 0.001, and $^{\#\#\#\#}P$ < 0.0001 *vs* the IRI group.

Crystal data for hyperhomanoon C (**3**): $C_{37}H_{46}O_6$, Mr = 586.74, a = 14.7130 (2) Å, b = 27.8857 (3) Å, c = 7.684 60 (10) Å, α = 90°, β = 90°, γ = 90°, V = 3152.86 (7) Å^3, T = 293 (2) K, space group P 21 212, Z = 4, μ(Cu Kα) = 0.657 mm $^{-1}$, θ_{max} = 73.867, 37693 reflections measured, 6318 independent reflections (R_{int} = 0.0333). The final R_1 values were 0.0690 [$I > 2\sigma(I)$]. The final $wR(F^2)$ values were 0.1957 [$I > 2\sigma(I)$]. The final R_1 values were 0.0714 (all data). The final $wR(F^2)$ values were 0.1988 (all data). The goodness of fit on F^2 was 1.076. Flack parameter = 0.11 (5).

3.4. *In vivo* activity evaluation

Male C57BL/6J wild-type mice (6–8 weeks old) were housed under standard laboratory conditions (22 °C, 50% relative humidity, 12-h light/dark cycle). All animal procedures were conducted in accordance with institutional guidelines and approved under ethical clearance number TJH-202208010. Compound **6** was administered intraperitoneally at a dose of 10 mg·kg^{-1} once a day for three consecutive days. On the third day, hepatic ischemia/reperfusion (I/R) surgery was performed 1 h after the final dose. Anesthesia was induced with sodium pentobarbital (80 mg·kg^{-1}, i.p.; Sigma, MO, USA), followed by a midline laparotomy. Ischemia was induced by clamping the arterial and portal venous inflow to the left and median liver lobes using an atraumatic vascular clip under microscopic guidance. After 60 min, the clip was removed to initiate reperfusion. Throughout the procedure, body temperature was maintained at 32 °C using a warming pad. Liver tissues were collected 6 h post-reperfusion for subsequent analyses. Sham-operated animals underwent identical surgical procedures except for vascular occlusion.

The plasma was collected from centrifuged blood specimens at 8000 r·min^{-1} for 10 min. The levels of ALT, AST, and LDH were analyzed across an automatic analyzer (Mindray Auto AnalyzerBS-200).

Histopathological and immunohistochemical evaluations were performed following established protocols [14, 45]. Liver tissues were fixed in 4% formalin, embedded in paraffin, and sectioned at 4 μm thickness. H&E staining was employed to assess liver morphology, and injury severity was scored blindly using Suzuki's criteria on a 0–4 scale. Apoptotic cells were detected by TUNEL staining, and cleaved caspase-3 expression was analyzed to confirm apoptosis. MPO expression was evaluated *via* immunohistochemistry to assess inflammatory infiltration. For each sample, three random microscopic fields were analyzed and used for quantitative evaluation.

Funding

This work was supported by the National Natural Science Foundation for Distinguished Young Scholars (No. 81725021) and the National Natural Science Foundation of China (Nos. 82003633 and 82173705).

Supplementary data

Supplementary data for this study can be obtained by contacting the corresponding authors *via* E-mail.

Declaration of competing interest

These authors have no conflict of interest to declare.

References

1 Fang B, Yang J, Wang L, et al. A mitochondria-targeted H_2S-activatable fluorogenic probe for tracking hepatic ischemia-reperfusion injury. *Chin Chem Lett*. 2024;35(6):108913. https://doi.org/10.1016/j.cclet.2023.108913.

2 Fang Y, Hu Q. Neutrophil CC1 plays a protective role in orthotopic liver transplantation: views from the perspective of natural compounds. *Chin J Nat Med*. 2023;21(4):241-242. https://doi.org/10.1016/S1875-5364(23)60432-7.

3 Hu H, Li Y, Shi Z, et al. Discovery of ergosterol derivative from *Aspergillus* sp. TJ507 that protects against hepatic ischemia/reperfusion injury. *Bioorg Chem*. 2023;135:106530. https://doi.org/10.1016/j.bioorg.2023.106530.

4 Jia Y, Xiao H, Wang X, et al. Design, synthesis, and evaluation of *n*-butylphthalide and ligustrazine hybrids as potent neuroprotective agents for the treatment of ischemic stroke *in vitro* and *in vivo*. *Bioorg Chem*. 2024;142:106961. https://doi.org/10.1016/j.bioorg.2023.106961.

5 Li S, Xu F, Yu L, et al. Stigmasterol protects human brain microvessel endothelial cells against ischemia-reperfusion injury through suppressing EPHA2 phosphorylation. *Chin J Nat Med*. 2023;21(2):127-135. https://doi.org/10.1016/S1875-5364(23)60390-5.

6 Liu H, Huang Z, Jiang H, et al. Dihydroartemisinin attenuates ischemia/reperfusion-induced renal tubular senescence by activating autophagy. *Chin J Nat Med*. 2023;21(9):682-693. https://doi.org/10.1016/S1875-5364(23)60398-X.

7 Liu J, Mu D, Xu J, et al. Inhibition of TLR4 signaling by isorhapontigenin targeting of the AHR alleviates cerebral ischemia/reperfusion injury. *J Agric Food Chem*. 2023;71(36):13270-13283. https://doi.org/10.1021/acs.jafc.3c00152.

8 Ma Y, Zhao C, Hu H, et al. Liver protecting effects and molecular mechanisms of icariin and its metabolites. *Phytochemistry*. 2023;215:113841. https://doi.org/10.1016/j.phytochem.2023.113841.

9 Qi Z, Tong Y, Luo H, et al. Neuroprotective effect of a Keap1-Nrf2 protein-protein inter-action inhibitor on cerebral ischemia/reperfusion injury. *Bioorg Chem*. 2023;132:106350. https://doi.org/10.1016/j.bioorg.2023.106350.

10 Sun Z, Wang Y, Pang X, et al. Mechanisms of polydatin against spinal cord ischemia–reperfusion injury based on network pharmacology, molecular docking and molecular dynamics simulation. *Bioorg Chem*. 2023;140:106840. https://doi.org/10.1016/j.bioorg.2023.106840.

11 Xue Y, Fu W, Yu P, et al. Ginsenoside Rc alleviates myocardial ischemia-reperfusion injury by reducing mitochondrial oxidative stress and apoptosis: role of SIRT1 activation. *J Agric Food Chem*. 2023;71(3):1547-1561. https://doi.org/10.1021/acs.jafc.2c06926.

12 Yang Z, Luo G, Ying Y, et al. Novel 2,6-disubstituted benzofuran-3-one analogues improve cerebral ischemia/reperfusion injury *via* neuroprotective and antioxidative effects. *Bioorg Chem*. 2023;132:106346. https://doi.org/10.1016/j.bioorg.2023.106346.

13 Zhang B, Chen Z, Jiang Z, et al. Nephroprotective effects of cardamonin on renal ischemia reperfusion injury/UUO-induced renal fibrosis. *J Agric Food Chem*. 2023;71(36):13284-13303. https://doi.org/10.1021/acs.jafc.3c01880.

14 Zhang Y, Zhao X, Cao Y, et al. Bioactive indole alkaloid from *Aspergillus amoenus* TJ507 that ameliorates hepatic ischemia/reperfusion injury. *J Nat Prod*. 2023;86(8):2059-2064. https://doi.org/10.1021/acs.jnatprod.3c00251.

15 Zhang F, Yang J, Yi P, et al. Hyperpatone A, a polycyclic polyprenylated acylphloroglucinol with a rare 8/6/5/6/5 pentacyclic skeleton from *Hypericum patulum*. *Org Biomol Chem*. 2022;21(1):140-146. https://doi.org/10.1039/d2ob01851a.

16 Li X, Li Q, Xu J, et al. Isolation and antihyperglycemic effects of garcibractinols A–H, intricate polycyclic polyprenylated acylphloroglucinols from the fruits of *Garcinia bracteata*. *Bioorg Chem*. 2023;138:106651. https://doi.org/10.1016/j.bioorg.2023.106651.

17 Huang JC, Xu HH, Shi Q, et al. Enantiomeric pairs of macrocyclic acylphloroglucinols from *Syzygium szemaoense*. *Bioorg Chem*. 2023;132:106381. https://doi.org/10.1016/j.bioorg.2023.106381.

18 Zhang R, Cheng Z, Fang Q, et al. Monoterpenoid acylphloroglucinols from *Hypericum hengshanense* W. T. Wang with antiproliferative activities. *Phytochemistry*. 2023;205:113500. https://doi.org/10.1016/j.phytochem.2022.113500.

19 Ye YS, Duan YT, Zhou Z, et al. Structurally diverse cytotoxic polyphenols from *Garcinia gracilis*. *J Nat Prod*. 2023;86(9):2206-2215. https://doi.org/10.1021/acs.jnatprod.3c00498.

20 Daus M, Hayton JB, Holland DC, et al. Camaldulensals A–C, the first meroterpenoids possessing two spatially separated formyl phloroglucinols conjugated to a terpene core from the leaves of *Eucalyptus camaldulensis* Dehnh. *J Nat Prod*. 2023;86(8):1994-2005. https://doi.org/10.1021/acs.jnatprod.3c00443.

21 Cuesta-Rubio O, Monzote L, Fernández-Acosta R, et al. A review of nemorosone: chemistry and biological properties. *Phytochemistry*. 2023;210:113674. https://doi.org/10.1016/j.phytochem.2023.113674.

22 Qiu YF, Grossman RB, Yang XW. Structure revision of type B polycyclic polyprenylated acylphloroglucinols fused to a partly reduced furan ring. *J Nat Prod*. 2023;86(10):2391-2397. https://doi.org/10.1021/acs.jnatprod.3c00591.

23 Xie JY, Wang ZX, Liu WY, et al. Hyperelatolides A–D, antineuroinflammatory constituents with unusual carbon skeletons from *Hypericum elatoides*. *J Nat Prod*. 2023;86(8):1910-1918. https://doi.org/10.1021/acs.jnatprod.3c00226.

24 Tan X, Qi C, Zhao X, et al. ERK inhibition promotes engraftment of allografts by reprogramming T-cell metabolism. *Adv Sci*. 2023;10:2206768. https://doi.org/10.1002/advs.202206768.

25 Qi C, Bao J, Wang J, et al. Asperterpenes A and B, two unprecedented meroterpenoids from *Aspergillus terreus* with BACE1 inhibitory activities. *Chem Sci*. 2016;7(10):6563-6572. https://doi.org/10.1039/C6SC02464E.

26 Duan Y, Guo Y, Deng Y, et al. Norprzewalsone A, a rearranged polycyclic polyprenylated acylphloroglucinol with a spiro[cyclopentane-1,3-tricyclo[7.4 $0.0^{1,6}$]tridecane] core from *Hypericum przewalskii*. *J Org Chem*. 2022;87(10):6824-6831. https://doi.org/10.1021/acs.joc.2c00503.

27 Duan Y, Bu P, Guo Y, et al. Walskiiglucinol A, a pair of rearranged acylphloroglucinol derivative enantiomers from *Hypericum przewalskii*. *Org Biomol Chem*. 2022;24(20):4970-4975. https://doi.org/10.1039/d2ob00562j.

28 Tian W, Qiu Y, Jin X, et al. Novel polycyclic polyprenylated acylphloroglucinols from *Hypericum sampsonii*. *Tetrahedron*. 2014;70(43):7912-7916. https://doi.org/10.1016/j.tet.2014.08.062.

29 Yang X, Li M, Liu X, et al. Polycyclic polyprenylated acylphloroglucinol congeners possessing diverse structures from *Hypericum henryi*. *J Nat Prod*. 2015;78(4):885-895. https://doi.org/10.1021/acs.jnatprod.5b00057.

30 Muñoz-Sánchez J, Chánez-Cárdenas ME. The use of cobalt chloride as a chemical hypoxia model. *J Appl Toxicol*. 2019;39(4):556-570. https://doi.org/10.1002/jat.3749.

31 Tang Q, Dai X, Lin Q, et al. Dcalycinumines A–E, alkaloids with cytotoxic activities of nasopharyngeal carcinoma cells from *Daphniphyllum calycinum*. *Chin J Chem*. 2024;42(1):35-42. https://doi.org/10.1002/cjoc.202300442.

32 Cheng Y, Li H, Wu D, et al. Anti-inffammatory polyoxygenated cyclohexene derivatives from *Uvaria macclurei*. *Phytochemistry*. 2023;214:113797. https://doi.org/10.1016/j.phytochem.2023.113797.

33 Zhang Y, Zeng M, Li B, et al. *Ephedra* herb extract ameliorates adriamycin-induced nephrotic syndrome in rats *via* the CAMKK2/AMPK/mTOR signaling pathway. *Chin J Nat Med*. 2023;21(5):371-382. https://doi.org/10.1016/S1875-5364(23)60454-6.

34 Liu Y, Li J, Gao H, et al. A near-infrared and lysosome-targeted BODIPY photosensitizer for photodynamic and photothermal synergistic therapy. *Org Biomol Chem*. 2023;21(22):4672-4682. https://doi.org/10.1039/d3ob00465a.

35 Samanta S, Maiti K, Halder S, et al. A 'double locked' ratiometric fluorescent probe for detection of cysteine in a viscous system and its application in cancer cells. *Org Biomol Chem*. 2023;21(3):575-584. https://doi.org/10.1039/d2ob01813f.

36 Duan D, He H, Ding W, et al. Site-selective C–H difunctionalization of *N*-alkyl activated azaarenes *via* the synergistic catalysis of graphene oxide and visible light. *Org Chem Front*. 2023;10:6055-6062. https://doi.org/10.1039/D3QO01375H.

37 Wang E, Han R, Wu M, et al. Size-dependent macrophage-targeting of mannose-modified rosiglitazone liposomes to alleviate inflammatory bowel disease. *Chin Chem Lett*. 2024;35(1):108361. https://doi.org/10.1016/j.cclet.2023.108361.

38 Zhu T, Zhao M, Wang R, et al. Hantzsch ester modified asymmetric BODIPY probe with ultra-high sensitivity for ultra-fast detection of endogenous hypochlorite in living cells. *Chin J Chem*. 2023;41(23):3319-3325. https://doi.org/10.1002/cjoc.202300345.

39 Kim H, Shil A, Sarkar S, et al. Dissecting the crosstalk between bisulffte and hypochlorous acid in the reaction-based fluorescence detection with dicyanovinyl based probes. *J Org Chem*. 2023;88(9):5563-5571. https://doi.org/10.1021/acs.joc.3c00086.

40 Zhang L, Gao J, Wang B, et al. Imine induced metal-free C–H arylation of indoles. *Org Chem Front*. 2023;10:6063-6069. https://doi.org/10.1039/D3QO01002C.

41 Duan Y, Sun W, Li Y, et al. Spirohypertones A and B as potent antipsoriatics: tumor necrosis factor-α inhibitors with unprecedented chemical architectures. *Acta Pharm Sin B*. 2024;14(6):2646-2656. https://doi.org/10.1016/j.apsb.2024.02.002.

42 Tao B, Li Y, Duan Y, et al. Discovery of adamantane-type polycyclic polyprenylated acylphloroglucinols that can prevent concanavalin A-induced autoimmune hepatitis in mice. *Bioorg Chem*. 2024;144:107145. https://doi.org/10.1016/j.bioorg.2024.107145.

43 Tao B, Li Y, Shi Z, et al. Discovery of bioactive polycyclic polyprenylated acylphloroglucinols with adamantine/homoadamantane skeletons from *Hypericum wilsonii*. *Phytochemistry*. 2024;218:113953. https://doi.org/10.1016/j.phytochem.2023.113953.

44 Shi Z, Zhao X, Song F, et al. Prenyllongnols A–D, new prenylated acylphloroglucinols that fight concanavalin A-induced autoimmune hepatitis. *J Agr Food Chem*. 2023;71(46):17801-17809. https://doi.org/10.1021/acs.jafc.3c05245.

45 Hu H, Li L, Shi Z, et al. Polyaspers A and B, the first ergosterol-polyether adducts with unprecedented 6/6/6/5/5/6/6/6/6 nonacyclic architecture from *Aspergillus* sp. TJ507. *Chin J Chem*. 2024;42(7):743-751. https://doi.org/10.1002/cjoc.202300649.